The resolution of whole Earth seismic tomographic models

G. Soldati[1] and L. Boschi[2]

[1]*Istituto Nazionale di Geofisica e Vulcanologia, Rome, Italy*
[2]*ETH, Zürich, Switzerland*

SUMMARY

We evaluate the resolution of whole Earth structure achieved by compressional wave traveltime data from the International Seismological Centre (ISC); the measure of resolution we employ, provided by the direct calculation of the model resolution matrix, is more rigorous than the traditional (and computationally cheaper) one obtained through synthetic/checkerboard tests. Our work completes the introductive study of Boschi (2003), where only mantle models derived with a very simple regularization scheme were considered. Here, we expand Boschi's database with measurements of compressional waves reflected by, or refracted through, the Earth's core–mantle boundary (CMB) and core. In analogy with the work of Soldati *et al.* (2003), we treat CMB topography and heterogeneous outer core structure as free parameters of our inversions; analysing model resolution matrices, we attempt to explain the known discrepancy between deep Earth structure mapped by seismic waves reflected and refracted by the core.

Key words: inverse theory, resolution, whole Earth tomography.

1 INTRODUCTION

The resolution of global seismic tomographic images of the Earth has often been evaluated through synthetic, or checkerboard, tests (e.g. Spakman & Nolet 1988). The limits of this approach, giving a measure of resolution which strongly depends on the choice of an 'input model', are known (e.g. Lévêque *et al.* 1993), but so far authors have stuck to it because it is computationally cheap. Modern computers, however, now allow more sophisticated data analyses, and Boschi (2003) has shown that the model resolution matrix (e.g. Menke 1989) can be efficiently computed for a global model of intermediate nominal resolution. The resolution matrix, **R**, can be thought of as the operator that relates output and input model in any synthetic test (independently of the input model), and knowing **R** is equivalent to knowing exactly what fictitious trade-offs (aliasing, leaking) occur, in the least-squares inversion, between any couple of model coefficients: obviously a much more comprehensive measure of resolution than any retrieved or not retrieved checkerboard.

Over the last two decades, several authors (Morelli & Dziewonski 1987; Pulliam & Stark 1993; Rodgers & Wahr 1993; Vasco & Johnson 1998; Boschi & Dziewonski 2000; Soldati *et al.* 2003; Sze & van der Hilst 2003; Vasco *et al.* 2003) have employed *PcP* (reflected by the CMB), *PKPbc/ PKPab* (refracted through CMB) and *PKPdf* (refracted through CMB and inner core boundary) traveltime observations to derive 'whole Earth' tomographic maps, including lateral heterogeneities in the CMB topography and outer core *P* velocity. Their results have systematically evidenced a discrepancy (first noted by Rodgers & Wahr 1993, in the context of CMB imaging only) between maps derived from *PcP* versus *PKP* data, for which no convincing explanation has yet been proposed.

In an attempt to explain those controversial results, we apply here the approach used by Boschi (2003) for resolution analysis to the problem of imaging the Earth's mantle, CMB and outer core structure by simultaneous inversions of *P*, *PcP* and *PKP* traveltime data. The database is that of Antolik *et al.* (2003), derived from the International Seismological Centre (ISC) bulletin after successive source relocations by Engdhal *et al.* (1998) and Antolik *et al.* (2003) themselves. While the robustness of mantle images is confirmed we find that the problem of mapping the Earth's CMB and core is inherently unstable, and suggest that no reliable model of those regions can be determined unless more sophisticated procedures are designed (to take account of high-frequency structure in the D'', full anisotropy, etc.).

We complete the work of Boschi (2003), where only a very simple norm-damping scheme was applied, with a careful analysis of the effects on resolution of different regularization criteria.

2 MEASURES OF RESOLUTION

The tomographic inverse problem is described by the equation

$$\mathbf{A} \cdot \mathbf{x} = \mathbf{d}, \tag{1}$$

where **d** denotes the data *m*-vector, **x** is the *n*-vector of solution coefficients and **A** is an $m \times n$ matrix whose entries depend on parametrization and data coverage (e.g. Boschi & Dziewonski 1999; Boschi 2001). Typically, eq. (1) is a mixed-determined problem, with $m \gg n$ but with very non-uniform data coverage (some model coefficients are not constrained). A simple formula exists for the damped least-squares solution of (1):

$$\mathbf{x}_{LS} = (\mathbf{A}^T \cdot \mathbf{A} + \mathbf{D})^{-1} \cdot \mathbf{A}^T \cdot \mathbf{d} \tag{2}$$
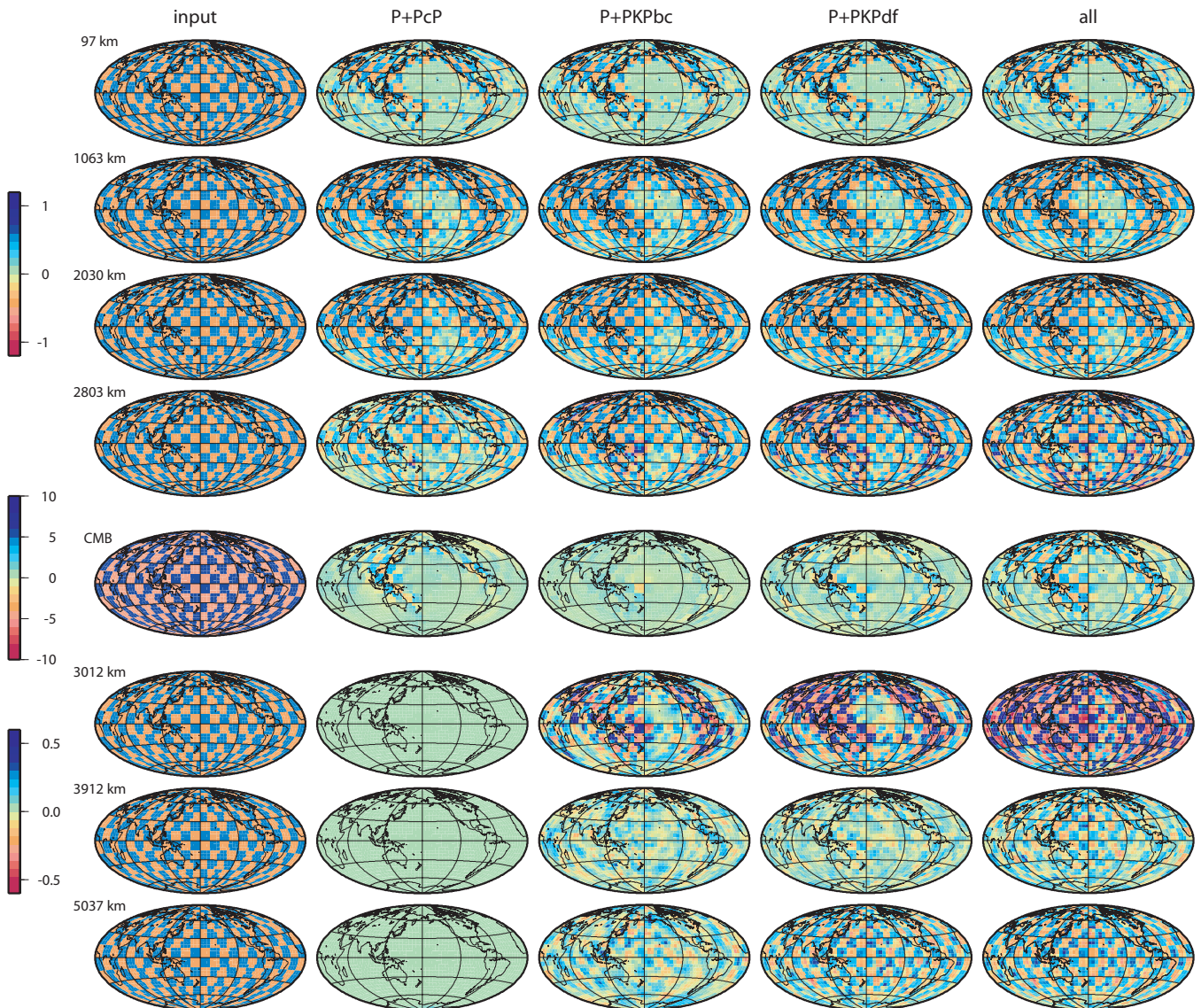
GJI Seismology

Figure 1. Checkerboard test with an input model (leftmost panels) of ±1 per cent mantle heterogeneities, ±10 km CMB topography and ±0.5 per cent outer core heterogeneities. Output models are derived (from left to right) from joint *P* and *PcP* data, *P* and *PKPbc* data, *P* and *PKPdf* data, and all data jointly inverted.

(e.g. Trefethen & Bau 1997), with **D** an $n \times n$ matrix describing the regularization (damping), and the superscript T denoting a transpose matrix.

We call 'resolution' the highest spatial frequency at which a tomographic image $\mathbf{x}_{LS}$ is expected to be meaningful, limited by the quality of the data and the adequacy of the parametrization (following Boschi 2003, we neglect the limits introduced by approximations in the theory). As we discuss below, resolution can be quantified in various ways.

2.1 Synthetic tests

Today, least-squares solutions in global tomography are usually computed via iterative (e.g. LSQR, SIRT, conjugate gradients) rather than direct (e.g. Cholesky factorization, singular value decomposition) algorithms (e.g. Trefethen & Bau 1997). Iterative algorithms are faster, but, owing to their approximate nature, provide less information about the inverse problem than direct algorithms do.

In practice, iterative algorithms involve the manipulation of the matrix **A**, rather than $\mathbf{A}^T \cdot \mathbf{A}$; this, as will shortly become evident, necessarily implies that resolution be evaluated through a 'synthetic test', rather than by rigorous analysis of the resolution matrix.

To perform a synthetic test, we first compute a synthetic data vector

$$\mathbf{d}_{syn} = \mathbf{A} \cdot \mathbf{x}_{in}, \tag{3}$$

associated with the 'input model' $\mathbf{x}_{in}$. We then replace **d** with $\mathbf{d}_{syn}$ in eq. (1), and apply our preferred algorithm to find the corresponding least-squares solution, which we call 'output model' $\mathbf{x}_{out}$. In principle, by repeating this exercise with input models of different spatial frequency (e.g. checkerboards, hence the term 'checkerboard test'), we can identify resolution.

We illustrate in Fig. 1 the outcome of a checkerboard test associated with the ISC database mentioned above (and to be used throughout the rest of this work), and a voxel parametrization (different from that employed below) of mantle, outer core and CMB
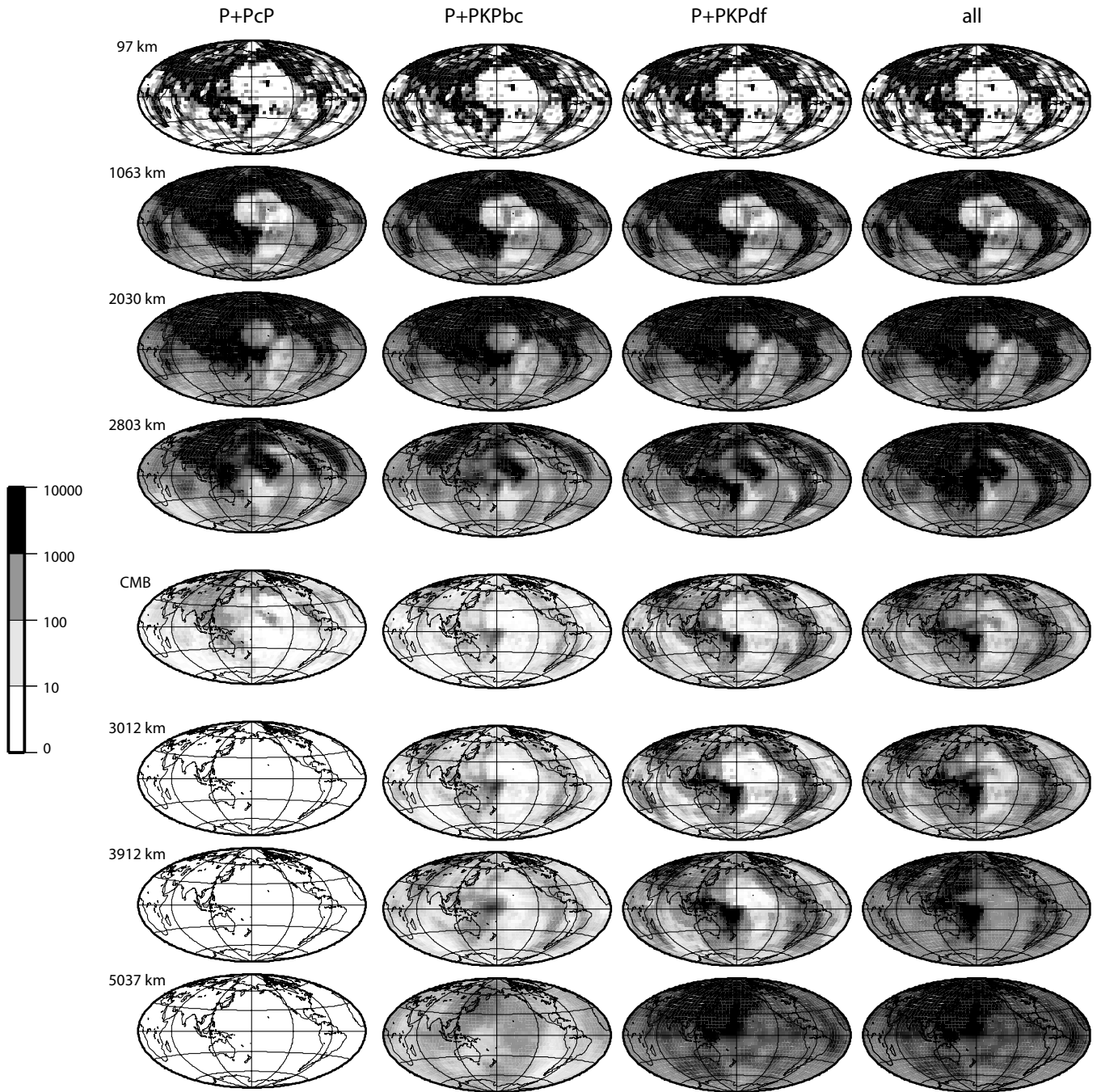
Figure 2. Number of ray paths, from the database of Antolik *et al.* (2003), crossing each voxel of our parametrization at several depths. From left to right, hit count plots of *PcP*, *PKPbc* and *PKPdf* subsets and the cumulative database (all images including *P*), respectively, are shown.

topography (e.g. Soldati *et al.* 2003). Fig. 1 shows resolution to be high in the mid and lower mantle, intermediate in the uppermost mantle (where teleseismic ray paths only cover regions close to sources and receivers), low in the outer core and very low at the CMB (the latter two regions being sampled only by *PKP* and *PcP* ray paths, far less numerous than direct *P*).

Boschi (2003) has shown the true limiting factor of resolution to be data noise rather than data coverage: the output model of Fig. 1 was derived with the same regularization scheme employed when inverting real data, necessary to suppress the effects of noise; undamped inversions of the same synthetic data result in $\mathbf{x}_{out}$ much more similar to $\mathbf{x}_{in}$.

In general, the similarity of $\mathbf{x}_{out}$ to $\mathbf{x}_{in}$ is strictly related to the data coverage; comparing Fig. 1 with the hit count map of Fig. 2, we contend that, in practice, synthetic tests do not provide much more information than a simple plot of data coverage. A more rigorous quantification of the fictitious interactions between model coefficients is needed (see also Lévêque *et al.* 1993).

2.2 Model resolution matrix

A formula relating input and output models is derived by replacing $\mathbf{d}$ with $\mathbf{d}_{syn}$ in eq. (2); then

$$\mathbf{x}_{out} = (\mathbf{A}^T \cdot \mathbf{A} + \mathbf{D})^{-1} \cdot \mathbf{A}^T \cdot \mathbf{A} \cdot \mathbf{x}_{in}, \tag{4}$$

we call $\mathbf{R} = (\mathbf{A}^T \cdot \mathbf{A} + \mathbf{D})^{-1} \cdot \mathbf{A}^T \cdot \mathbf{A}$ the model resolution matrix (e.g. Menke 1989): the similarity of $\mathbf{R}$ to the identity matrix is a measure of resolution, not depending on $\mathbf{x}_{in}$.

Iterative least-squares algorithms implement (2), and (4), implicitly; direct least-squares algorithms involve the explicit calculation of $\mathbf{A}^T \cdot \mathbf{A}$ and its inverse (or damped inverse): only by employing a direct algorithm, then, can we use $\mathbf{R}$ to evaluate model resolution.

The limiting case of perfect resolution (at the wavelength defined by the model parametrization) corresponds to $\mathbf{R}$ coinciding with the identity matrix: no model coefficients map into each other, and all the input model coefficients would be recovered perfectly in any synthetic test, independently of $\mathbf{x}_{in}$. If $R_{ij} \neq 0$, a fictitious coupling exists between the ith and jth model coefficients, namely

$$x_{out,i} = R_{ii}x_{in,i} + R_{ij}x_{in,j}; \qquad (5)$$

clearly, the larger R_{ij}, the stronger the trade-off, the lower the resolution.

It should be noted at this point that, while the matrix $\mathbf{A}^T \cdot \mathbf{A}$ is necessarily symmetric and positive-definite, there is no requirement for $\mathbf{R}$ to be symmetric; in practice, if the model coefficient x_i is constrained by a large number of reliable data and x_j is not, and the few noisy data that constrain x_j are also sensitive to x_i, it is likely that the value of x_j will depend fictitiously on that of x_i, but not vice versa; we shall then have R_{ij} close to zero, but R_{ji} significantly different from zero. This is the case when P and PcP or PKP data are inverted jointly, to map simultaneously the Earth's mantle (well constrained by the large P database) and CMB topography (only constrained by the PcP or PKP subsets, which are also very sensitive to mantle velocities).

3 THE RESOLUTION OF WHOLE EARTH TOMOGRAPHIC MODELS

3.1 Method

In previous work (Boschi & Dziewonski 2000; Soldati *et al.* 2003), we have derived seismic maps of the Earth's mantle, CMB and outer core parametrized in terms of 25 layers of 1656 voxels each (plus 1656 pixels to describe the CMB topography).

The more expensive resolution analysis carried out here suggests that, for the time being, a more compact parametrization be employed; like Antolik *et al.* (2003), we describe the horizontal velocity variations, and CMB topography, in terms of 362 equally spaced spherical splines (Wang & Dahlen 1995) and 28 equally spaced radial cubic B splines (20 for the mantle, eight for the outer core).

Splines are more efficient than voxels in representing relatively smooth functions, so the order-of-magnitude decrease in the number of free parameters is, to some extent, justified (Lancaster & Šalkauskas 1986).

We compute $\mathbf{x}_{LS}$ and $\mathbf{R}$ by Cholesky factorization of $\mathbf{A}^T \cdot \mathbf{A} + \mathbf{D}$; Cholesky factorization is known to be the most efficient direct
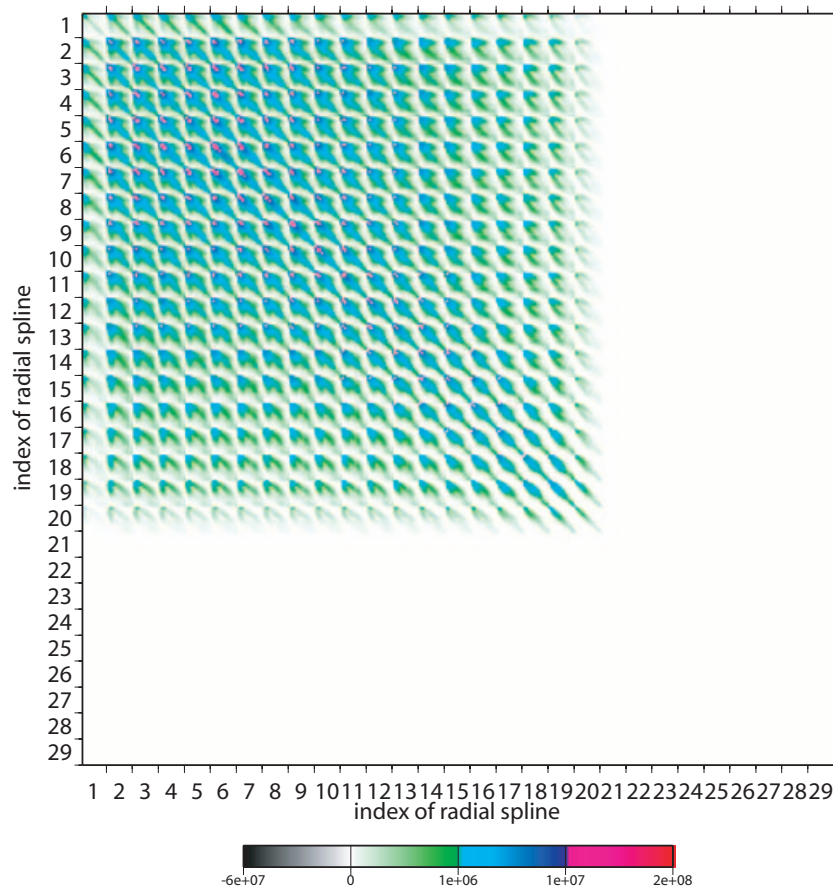

Figure 3. Averaged $\mathbf{A}^T \cdot \mathbf{A}$ matrix derived from P-wave data. Each row/column of $\mathbf{A}^T \cdot \mathbf{A}$ corresponds to a radial spline-horizontal spline couple; within each row/column entries are grouped by radial splines. The radial splines are indexed from shallowest (1) to deepest (29), where the first 20 radial splines describe the mantle, the 21st the CMB topography, and the following eight the outer core. The transition zone at ∼660 km corresponds roughly to the fifth radial spline. Since $\mathbf{A}^T \cdot \mathbf{A}$ is too large to be plotted entirely on one figure, for each 29 × 29 block of $\mathbf{A}^T \cdot \mathbf{A}$ we sum all entries and divide the result by 29.
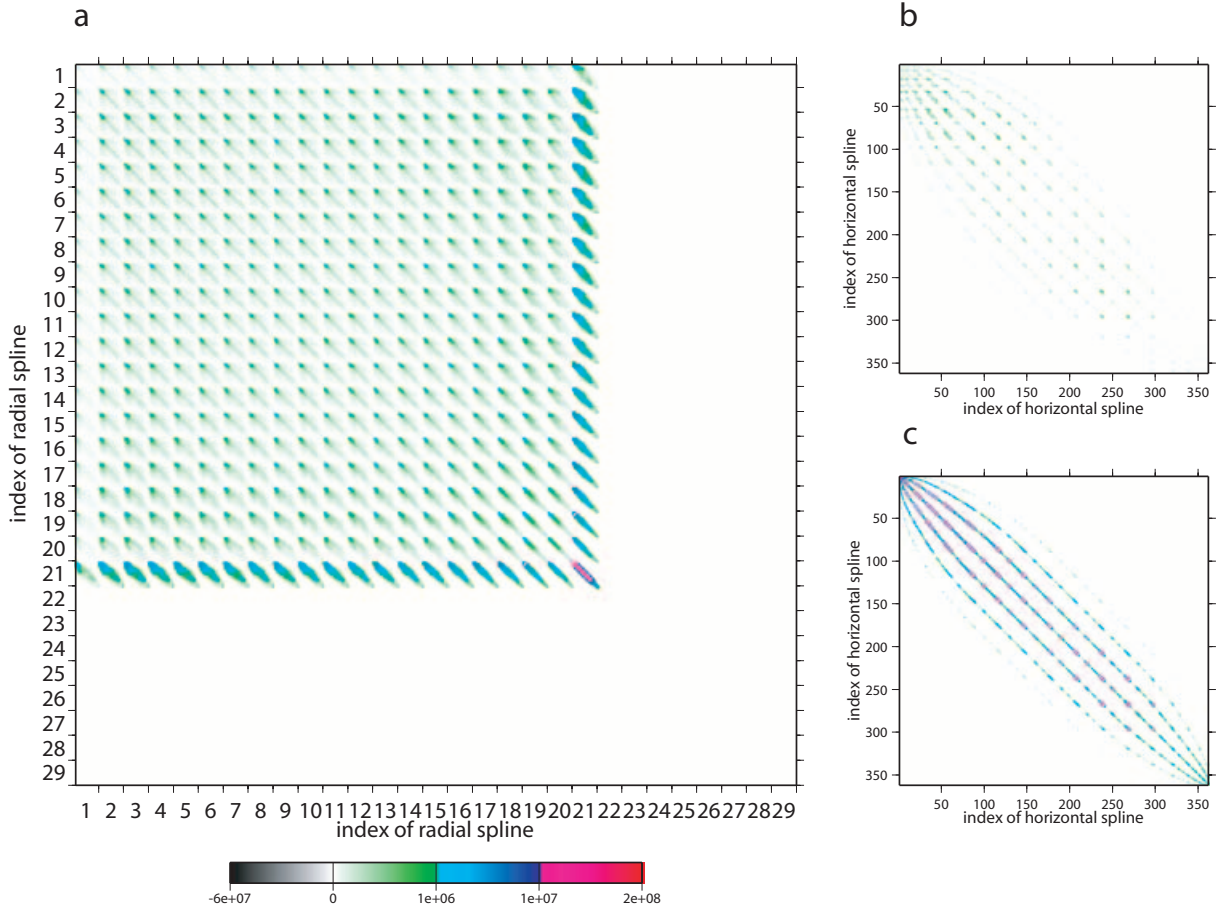
a

b

c

Figure 4. (a) Averaged $\mathbf{A}^T \cdot \mathbf{A}$ matrix from *PcP* data. The 21st radial spline describes the CMB topography. Right panels show the non-averaged plots of two specific blocks of the $\mathbf{A}^T \cdot \mathbf{A}$ matrix. Panel (b) refers to block (21,1): each entry of this block equals the product of the coefficient of one of the basis functions associated with the (shallowest) radial spline, times one of CMB coefficients. Panel (c) displays block (21,21), describing the interaction between CMB coefficients.

inversion algorithm (Press *et al.* 1992; Trefethen & Bau 1997). We compute both $\mathbf{A}$ and $\mathbf{A}^T \cdot \mathbf{A}$, and apply LSQR (Paige & Saunders 1982) to $\mathbf{A}$, as an additional internal consistency check. The least-squares solutions derived, with the same regularization scheme, from LSQR and Cholesky factorization are substantially coincident, and we infer that the factorization of $\mathbf{A}^T \cdot \mathbf{A}$ does not, as sometimes suggested, exacerbate the problem of errors mapping from the data into fictitious features of the solution (see also Boschi & Dziewonski 1999; Boschi 2001).

3.2 The matrix $\mathbf{A}^T \cdot \mathbf{A}$

The algorithm we have designed scans the database and computes $\mathbf{A}$ row by row, while at the same time updating each entry of $\mathbf{A}^T \cdot \mathbf{A}$. Entries of $\mathbf{A}$ and $\mathbf{A}^T \cdot \mathbf{A}$ are related by the equation

$$(\mathbf{A}^T \cdot \mathbf{A})_{ij} = (\mathbf{A}^T)_{ik} A_{kj} = A_{ki} A_{kj} \qquad (6)$$

(with implicit summation over the repeated index k), stating that the ij entry of $\mathbf{A}^T \cdot \mathbf{A}$ equals the dot product of the ith and jth columns of $\mathbf{A}$.

Each row of $\mathbf{A}$ is associated with one and only one datum, while each of its columns corresponds to one model coefficient; then, if two model coefficients are constrained by similar subsets of the database, we should expect approximately the same entries of the

two corresponding columns of $\mathbf{A}$ to be non-zero, and, consequently, their dot product to be relatively high. We infer that $(\mathbf{A}^T \cdot \mathbf{A})_{ij} \gg 0$ is a necessary (not sufficient) condition for the ith and jth model coefficients to be fictitiously coupled.

Before discussing $\mathbf{R}$ in the next section, we show examples of the matrix $\mathbf{A}^T \cdot \mathbf{A}$ in Fig. 3 (direct *P*-wave data only), Fig. 4 (*PcP*) and Fig. 5 (*PKPdf*). To display the entire $\mathbf{A}^T \cdot \mathbf{A}$ matrix in a single plot, we average its neighbouring entries (corresponding to the same radial spline), so that only vertical coupling is visible.

As expected, coupling from *P* data (Fig. 3) appears to be more relevant in the upper mantle (small radial spline indices), where their coverage is more non-uniform and the resolution lower (Boschi 2003). At larger depths, energy is more concentrated along the diagonal. The size of entries of $\mathbf{A}^T \cdot \mathbf{A}$ associated with the shallowest and deepest splines is systematically small, reflecting the difficulties of employing a spline parametrization near a boundary (Fig. 1b of Antolik *et al.* 2003).

Fig. 4 shows a quite different scenario, evidencing the sensitivity of *PcP* data to the CMB topography, and their likely inadequacy to constrain mantle structure (energy away from the diagonal of $\mathbf{A}^T \cdot \mathbf{A}$) unless combined with the *P* database. The structure of the entire mantle is likely to be affected by coupling with CMB topography; model coefficients in the lowermost mantle might be coupled with CMB undulations at the same location (nearly diagonal
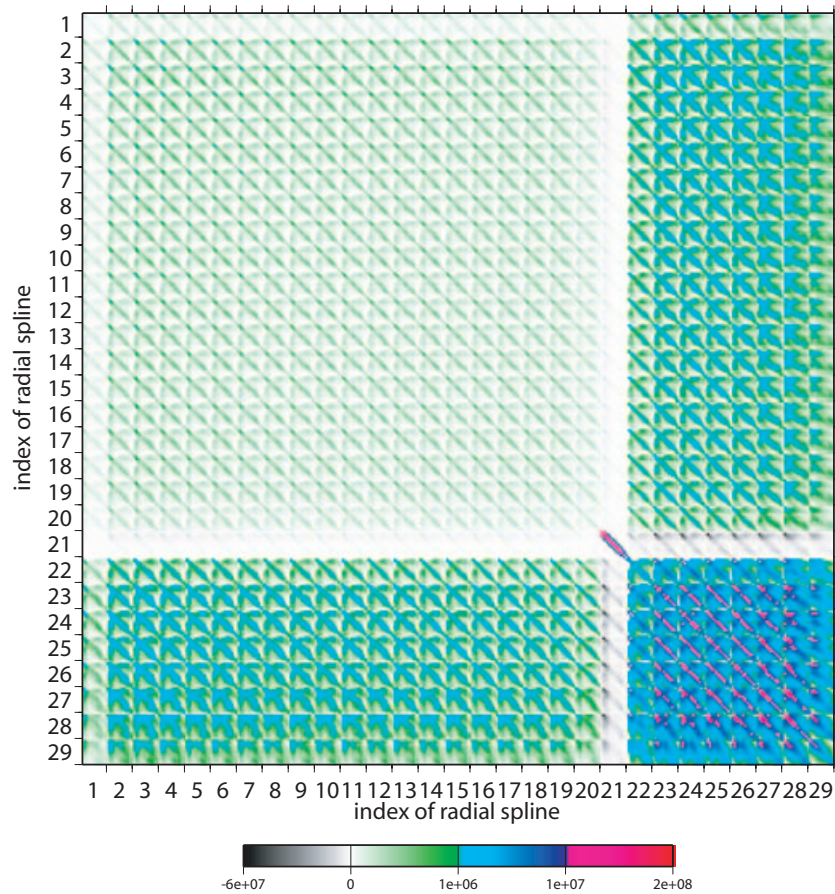
Figure 5. Averaged $\mathbf{A}^{\mathrm{T}} \cdot \mathbf{A}$ from *PKPdf* data.

blocks of $\mathbf{A}^{\mathrm{T}} \cdot \mathbf{A}$), while at shallower depths velocity anomalies over a larger volume might be affected.

Fig. 4 also includes, in its right panels, non-averaged plots of two specific blocks of $\mathbf{A}^{\mathrm{T}} \cdot \mathbf{A}$ (blocks (21,1) and (21,21), where radial splines 1 and 21 correspond respectively to the outermost layer of the mantle and to the CMB): off-diagonal non-zero fringes indicate the potential coupling between coefficients of neighbouring splines.

Lastly, Fig. 5 suggests that *PKPdf* data are also, most likely, inadequate to resolve mantle structure, introduce a smaller coupling between mantle and CMB structure, but are also probably insufficient to resolve CMB topography, its coefficients being strongly coupled with those describing the outer core.

3.3 The resolution matrix

From simple plots of $\mathbf{A}^{\mathrm{T}} \cdot \mathbf{A}$ we can speculate which model coefficients might be affected by strong fictitious trade-offs; computing the resolution matrix $\mathbf{R}$ is equivalent to finding the exact extent of such trade-offs, for any couple of model coefficients.

Boschi (2003) has discussed the resolution matrix associated with the problem of inverting ISC *P* traveltimes for mantle structure, and found that, after a sufficient norm damping is applied to suppress the effect of noise, a stable solution model can be derived without excessively strong trade-offs. Here, we shall rather focus on the resolution of CMB topography and outer core structure achieved from the cumulative *P*, *PKP* and *PcP* database.

To complete the treatment of Boschi (2003), we first show in Fig. 6 the effects of horizontal roughness damping of mantle structure; our long-wavelength parametrization involves a strong implicit smoothing, and it is thus not surprising that the map at the top right of Fig. 6 is very similar to the 'successful' model of Boschi (2003), where only norm damping was applied. The corresponding plots of $\mathbf{R}$ (whole matrix to the left, non-averaged blocks corresponding to $\sim$1450 km depth in Fig. 7) show that no particularly strong trade-off is introduced between the mantle and outer core/CMB, vertical trade-offs in the mantle are comparable to those of the images of Boschi (2003), and horizontal trade-offs are limited, for each horizontal spline, to the few closest neighbouring splines in the grid.

As the roughness is minimized more strongly (bottom panels) $\mathbf{R}$ deteriorates, with energy leaking over a broader area; more interestingly, a trade-off appears between mantle and outer core, where signal from the overdamped mantle gets fictitiously mapped (note the asymmetry of $\mathbf{R}$).

Fig. 8 illustrates the problems we are encountering when imaging the CMB topography. If this feature is left undamped, we obtain an unrealistic topography with very high lateral gradients (top panel); as we perform further inversions, emphasizing increasingly the minimization of the CMB norm with respect to other damping constraints (middle and bottom panels), the data signal associated with CMB topography is forced to leak into both mantle and outer core structure (note, again, the strong asymmetry of $\mathbf{R}$); naturally, the extent of this effect is proportional to the relative weight assigned to CMB damping, but is considerable even if the damping is
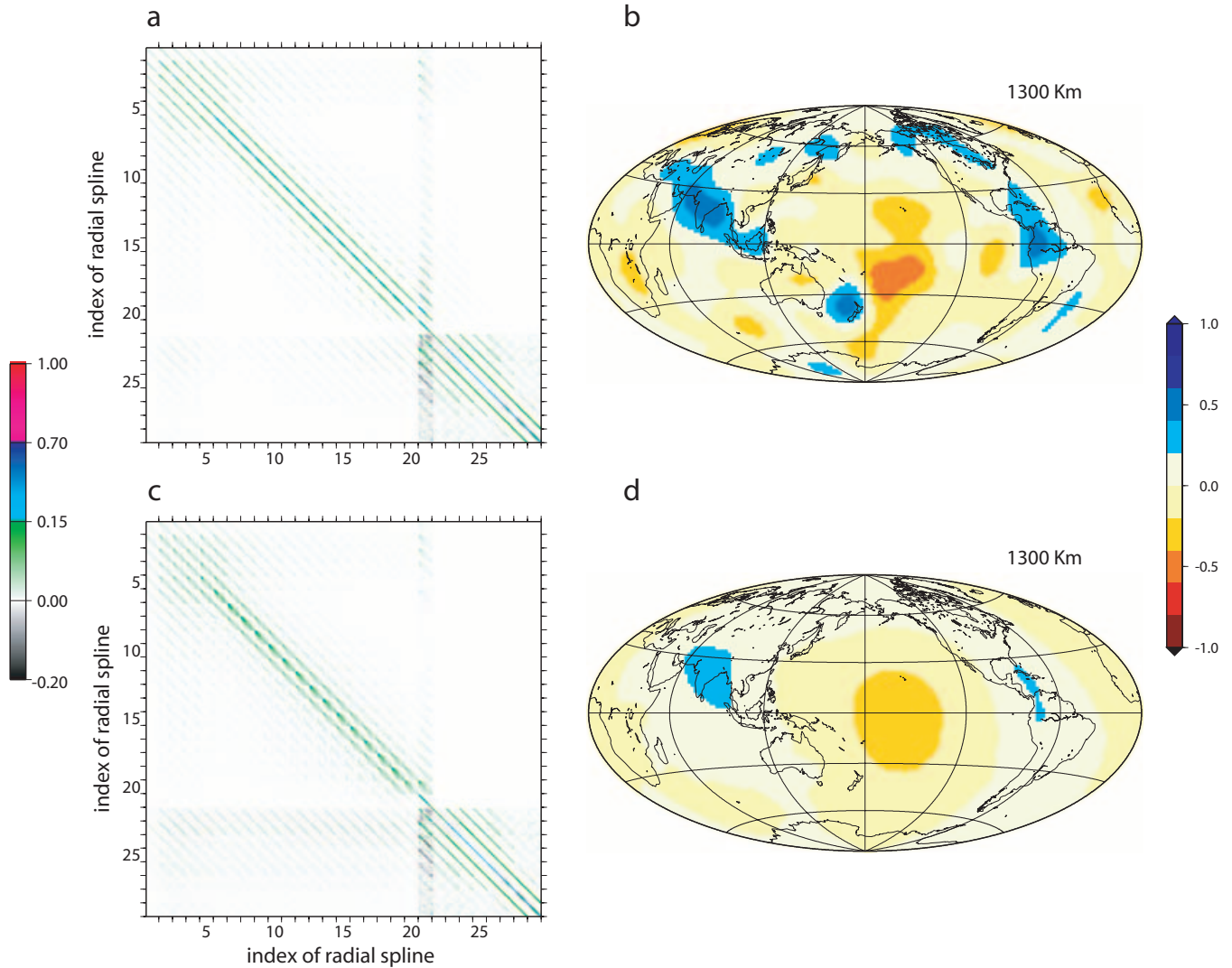
Figure 6. The effect of horizontal roughness damping, applied to mantle structure only, on the resolution matrix (panels a, c) and tomographic images (panels b, d, shown at 1300 km depth only) derived from the entire database. The model and **R** displayed at the bottom are derived applying a horizontal damping factor 25 times bigger than their counterparts at the top of the figure; other damping parameters are left unchanged. Relative velocity heterogeneities range between −1 and 1 per cent.

weak, and the mapped CMB topography still fairly rough (middle panel). It is also evident from Fig. 8 (and for tomographic images of mantle and outer core, not shown here), that changes in CMB damping affect (deteriorate) the mapped outer core much more than mantle structure.

We show in Fig. 9 the effects of varying the damping parameter associated with norm minimization of the outer core velocity, while leaving all the other parameters unchanged. As to be expected, when the outer core minimization constraint is weak, part of the signal associated with both mantle and CMB naturally tends to map into the outer core; again, outer core model coefficients are affected much more than mantle ones.

Images of **R** are hard to interpret unless linked to the geographical distribution of splines. Each column of Fig. 10 represents one selected row of **R**. To associate the coefficients of **R** to geographical locations, we plot for the three chosen values of i (the three selected rows of **R**) the quantity $\sum_{j=1}^{n} R_{ij} B_j(z, \theta, \phi)$, ($B_j$ denoting the jth basis function of our parametrization, the product of one radial spline and one horizontal spline) at some selected depths

in the mantle. Note that in the ideal case of perfect resolution, $\sum_{j=1}^{n} R_{ij} B_j(z, \theta, \phi) = B_i(z, \theta, \phi)$, and Fig. 10 would simply show three of our basis functions.

The chosen values of i correspond to horizontal splines roughly centred in (a) North America, (b) Japan and (c) the India/Eurasia boundary (all these are regions where deep fast anomalies are often imaged), and radial splines centred at (a) 500 km, (b) 1000 km and (c) 1500 km. The combination of a relatively long-wavelength parametrization and regularization needed to filter out data noise limits horizontal resolution to ∼2000 km; in the radial direction trade-offs are more limited, with a resolution of ∼500 km.

4 CONCLUSIONS

We have derived resolution matrices associated with a database of P, PKP and PcP traveltimes based on the ISC bulletins, for a large number of differently regularized tomographic inversions of (isotropic) mantle, core and CMB structure.
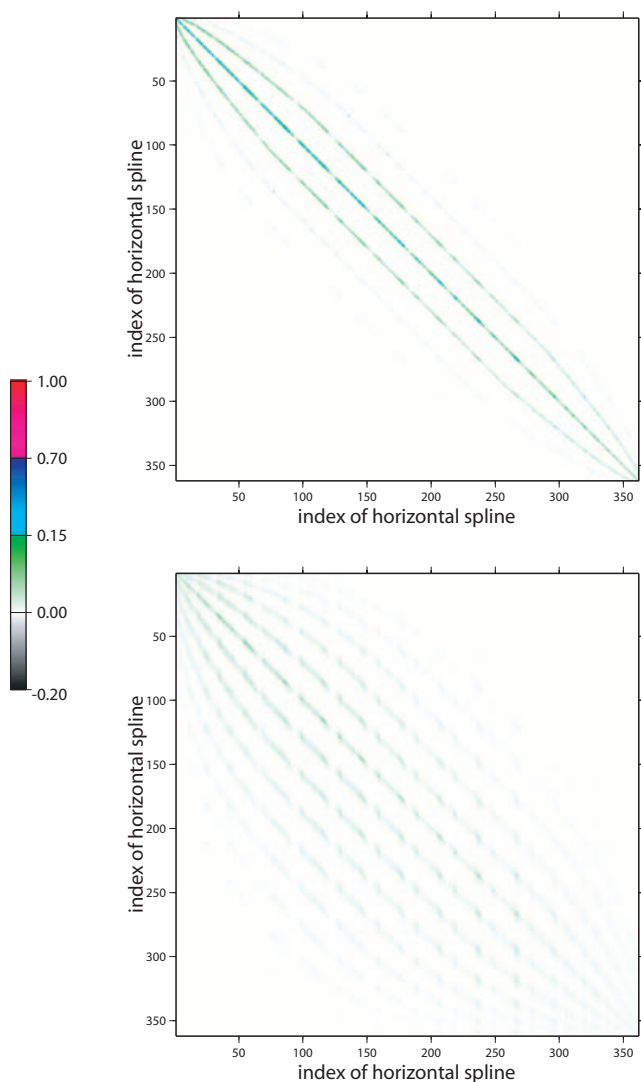
Figure 7. Tenth diagonal block of the resolution matrices in Fig. 6 (panels a, c), without averaging, showing the trade-off between coefficients of horizontal splines associated to the tenth radial spline (depth ∼1450 km).

Our treatment is similar to that of Boschi (2003), but complicated by the more complex nature of the problem: while all observations in our database are sensitive to mantle structure, only a subset are sensitive to CMB topography, and an even smaller subset can be used to image the outer core. *P* traveltimes, associated with ray paths travelling through the mantle only, are the most numerous and less noisy; *PcP* phases, reflected by the CMB, might have been confused with diffracted phases, giving rise to systematic errors over which we have no control; and *PKP* data are also generally more noisy, and far less numerous, than direct *P* ones.

As a general rule, we found fictitious trade-offs to be more severe within the CMB and outer core, or between the two, while imaged mantle structure remains relatively stable with respect to changes in regularization and in the inverted database. Naturally, the nature of trade-offs is strictly related to the damping schemes applied to the various portions of the solution.

The main goal of this study was to illustrate comprehensively the resolution-matrix approach to evaluation of resolution in global

tomography, applying the procedure of Boschi (2003) to a more complicated inverse problem. We have performed all calculations on a powerful shared-memory, multiprocessor computer, never taking full advantage of its large RAM; this, and the speed with which the Cholesky factorization is carried out (a few minutes), suggest that a refinement of our parametrization might be in order. It will be the subject of further work, attempting to isolate from traveltime measurements of core-reflected and refracted phases information about the deepest interior of the Earth.

REFERENCES

Antolik, M., Gu, Y. J., Ekström, G. & Dziewonski, A.M., 2003. J362D28: A new joint model of compressional and shear wave velocity in the Earth's mantle, *Geophys. J. Int.,* **153,** 443–466.

Boschi, L., 2001. Applications of linear inverse theory in modern global seismology, *Thesis,* Harvard University, Cambridge, MA.

Boschi, L., 2003. Measures of resolution in global body wave tomography, *Geophys. Res. Lett.,* **30,** doi:10.1029/2003GL018222.

Boschi, L. & Dziewonski, A.M., 1999. 'High' and 'low' resolution images of the Earth's mantle: implications of different approaches to tomographic modeling, *J. geophys. Res.,* **104,** 25 567–25 594.

Boschi, L. & Dziewonski, A.M., 2000. Whole Earth tomography from delay times of P, PcP, and PKP phases: Lateral heterogeneity in the outer core or radial anisotropy in the mantle?, *J. geophys. Res.,* **105,** 13 675–13 696.

Engdhal, E.R., van der Hilst, R.D. & Buland, R.P., 1998. Global teleseismic earthquake relocation with improved travel times and procedures for depth determination, *Bull. seism. Soc. Am.,* **88,** 722–743.

Lancaster, P. & Šalkauskas, K., 1986. *Curve and Surface Fitting—An Introduction,* Academic Press, San Diego, CA.

Lévêque, J.J., Rivera, L. & Wittlinger, G., 1993. On the use of checker-board test to assess the resolution of tomographic inversions, *Geophys. J. Int.,* **115,** 313–318.

Menke, W., 1989. *Geophysical Data Analysis: Discrete Inverse Theory,* revised edn, Academic Press, San Diego, CA.

Morelli, A. & Dziewonski, A.M., 1987. Topography of the core–mantle boundary and lateral homogeneity of the liquid core, *Nature,* **325,** 678–683.

Paige, C. & Saunders, M., 1982. LSQR: an algorithm for sparse linear equations and sparse least squares, *ACM Trans. Math. Software,* **8,** 43–71.

Press, W.H., Teukolsky, S.A., Vetterling, W.T. & Flannery, B.P., 1992. *Numerical Recipes in Fortran,* 2nd edn, Cambridge University Press, Cambridge.

Pulliam, R.J. & Stark, P.B., 1993. Bumps on the core–mantle boundary; are they facts or artifacts?, *J. geophys. Res.,* **98,** 1943–1955.

Rodgers, A. & Wahr, J., 1993. Inference of core-mantle boundary topography from ISC *PcP* and *PKP* travel times, *Geophys. J. Int.,* **115,** 991–1011.

Soldati, G., Boschi, L. & Piersanti, A., 2003. Outer core density heterogeneity and the discrepancy between *PKP* and *PcP* travel time observations, *Geophys. Res. Lett.,* **30,** doi:10.1029/200GL016647.

Spakman, W. & Nolet, G., 1988. Imaging algorithms, accuracy, and resolution in delay time tomography, in *Mathematical Geophysics,* pp. 155–188, eds Vlaar, N.J., Nolet, G., Wortel, M.J.R. & Cloething, S.A.P.L., Reidel, Dordrecht.

Sze, E.K.M. & van der Hilst, R.D., 2003. Core mantle boundary topography from short period *PcP*, *PKP*, and *PKKP* data, *Phys. Earth planet. Int.,* **135,** 27–46.

Trefethen, L.N. & Bau, D., 1997. *Numerical Linear Algebra,* SIAM, Philadelphia, PA.

Vasco, D.W., Johnson, L.R. & Marques, O., 2003. Resolution, uncertainty, and whole Earth tomography, *J. geophys. Res.,* **108,** doi:10.109/ 2001JB000412.

Vasco, D.W. & Johnson, L.R., 1998. Whole Earth structure estimated from seismic arrival times, *J. geophys. Res.,* **103,** 2633–2671.

Wang, Z. & Dahlen, F.A., 1995. Spherical-spline parameterization of three-dimensional Earth models, *Geophys. Res. Lett.,* **22,** 3099–3102.
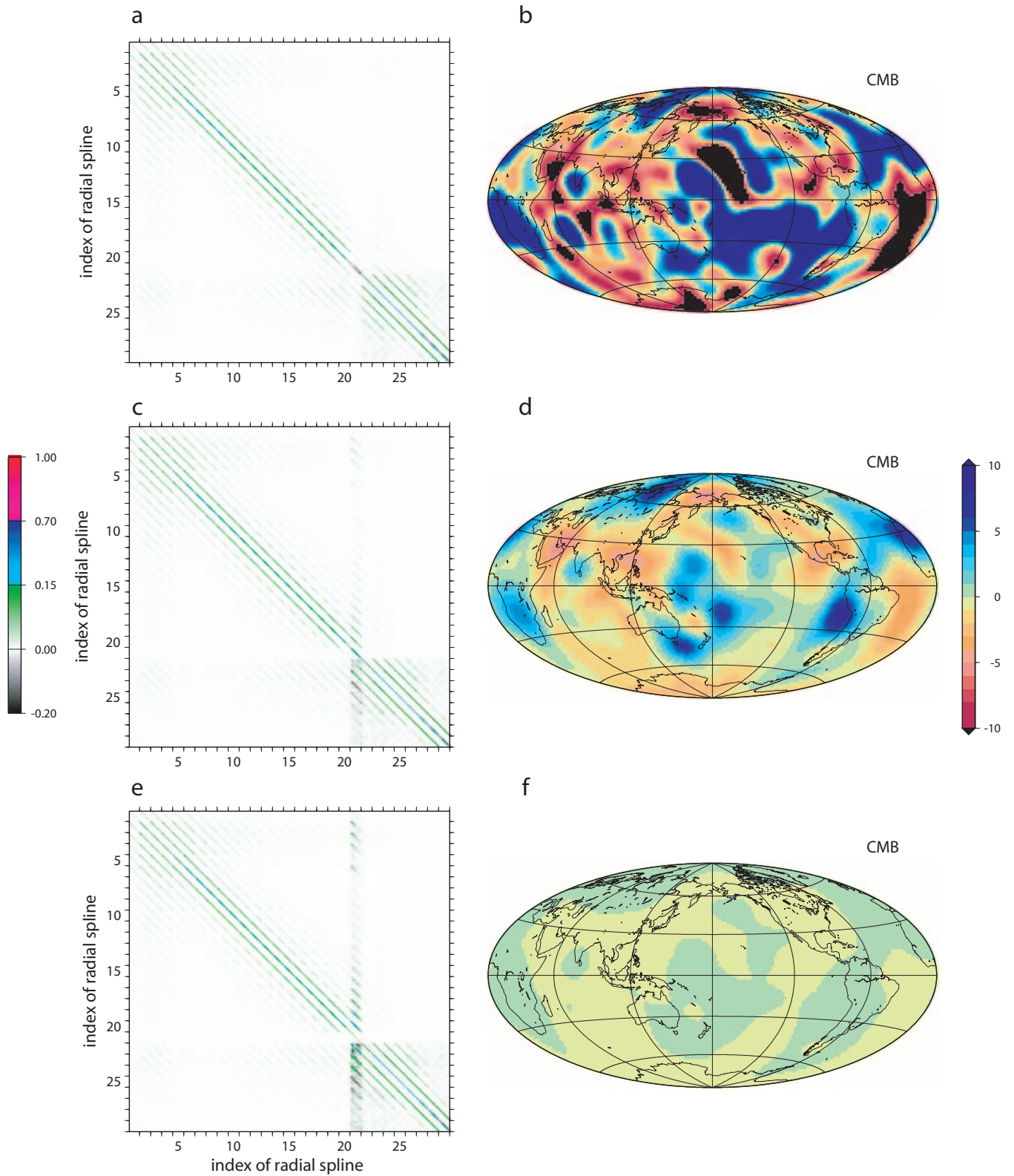
Figure 8. The effect of CMB norm damping on **R** (left) and on CMB topography maps (right). The corresponding damping parameter is increased 40 times from panels a, b to panels c, d, and 1000 times from panels a, b to panels e, f. The colour scale saturates for topography bigger than 10 km in absolute value.
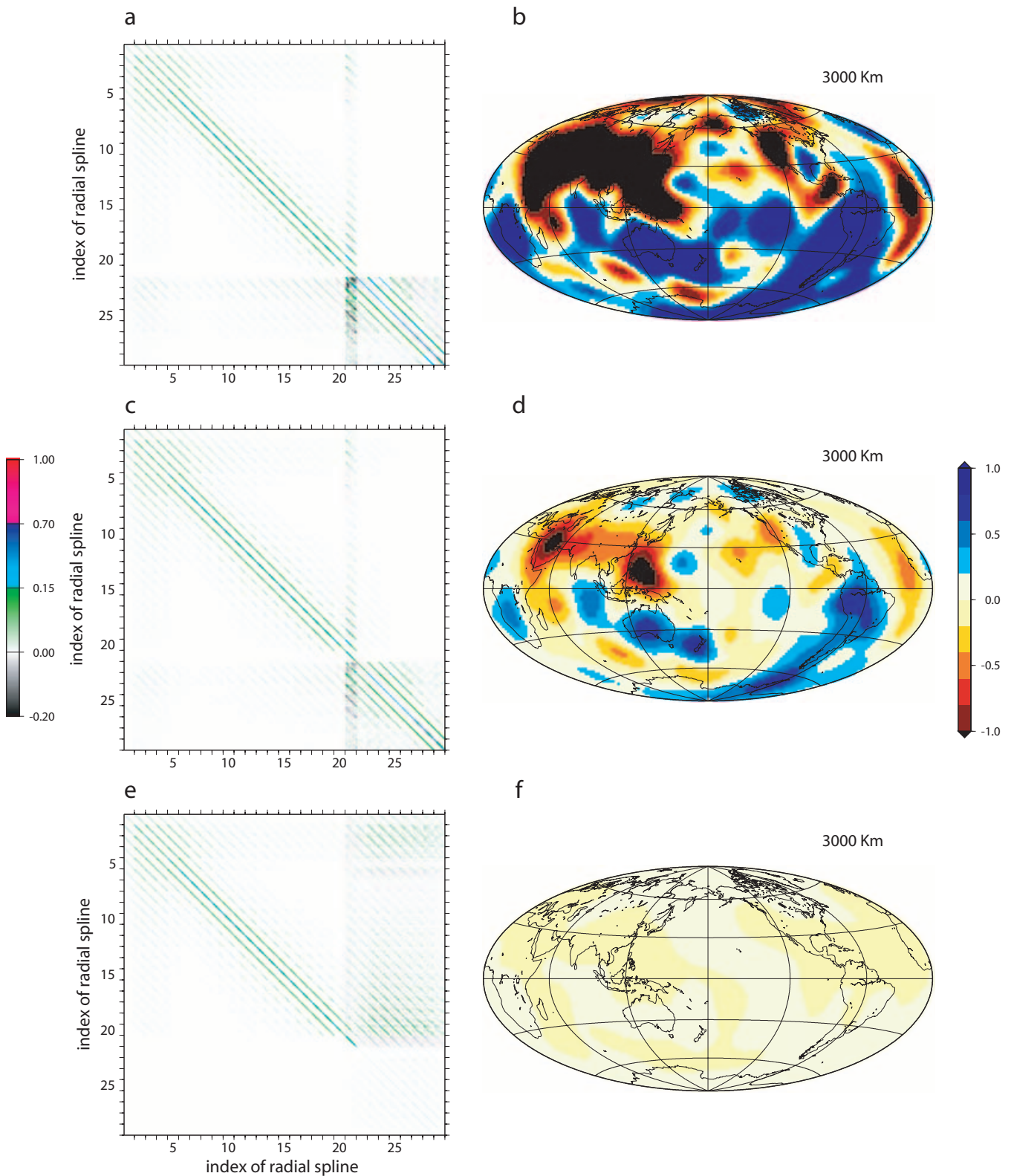
Figure 9. The effect of outer core norm damping on **R** (left) and outer core velocity heterogeneities (right). The corresponding damping parameter is increased 10 times from panels a, b to panels c, d, and 10 000 times from panels a, b to panels e, f. The color scale saturates for heterogeneities >1 per cent in absolute value.
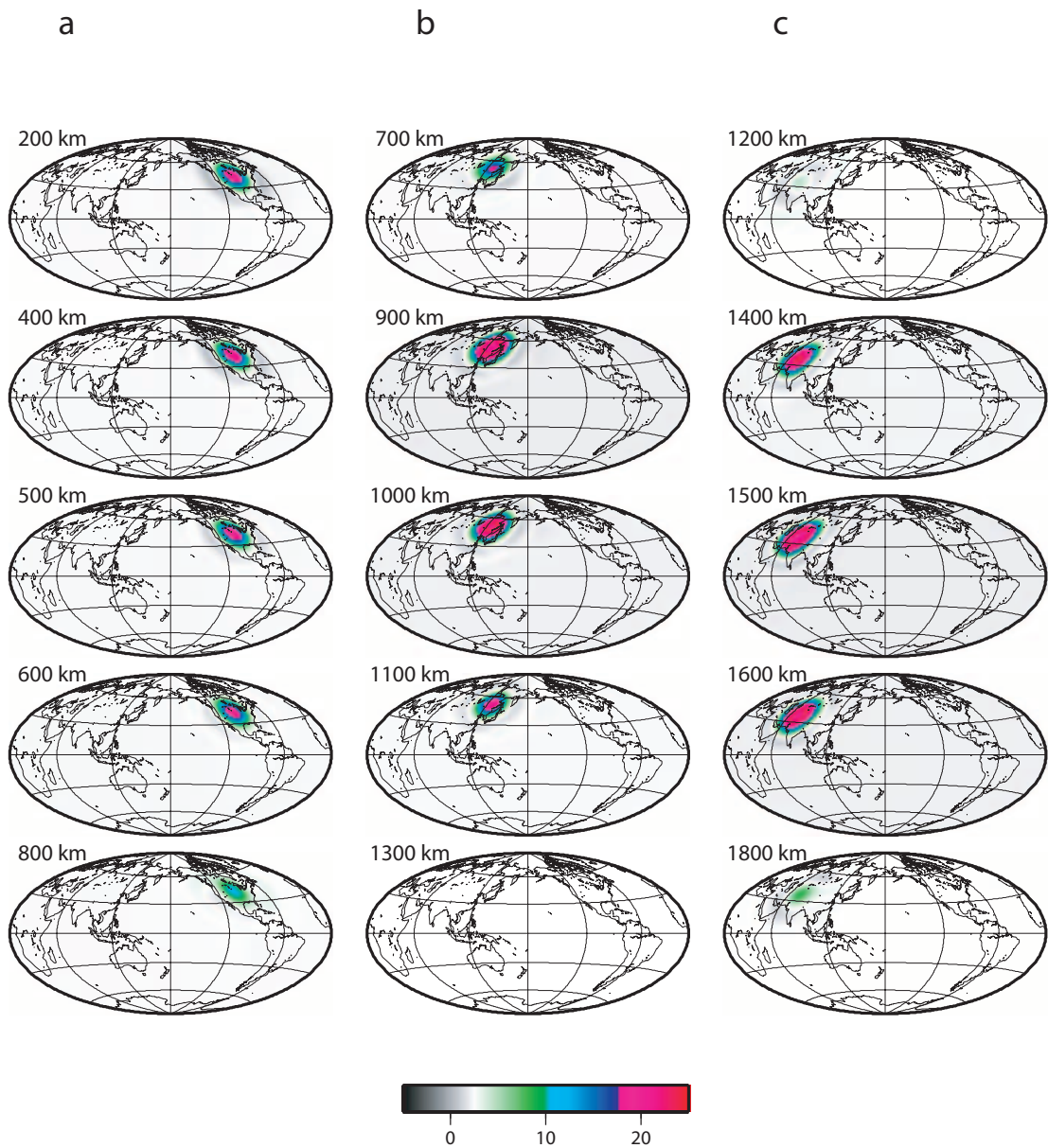
a   b   c

Figure 10. Geographical representation of the fictitious coupling of three selected basis functions (centred in (a) North America, (b) Japan, (c) the India/Eurasia boundary, at a depth of (a) 500 km, (b) 1000 km and (c) 1500 km) with the rest of the parametrization. For each basis function i, the plots represent the quantity $\sum_{j=1}^{n} R_{i\,j} B_j(z, \theta, \phi)$, B_j denoting the jth basis function of our parametrization.